International Journal of Modern Physics B
Vol. 31, No. 24 (2017) 1740007 (15 pages)

DOI: 10.1142/S0217979217400070

World Scientific
www.worldscientific.com

Plasmonics simulations including nonlocal effects using a boundary element method approach

Andreas Trügler* and Ulrich Hohenester

Institute of Physics, University of Graz,
Universitätsplatz 5, 8010 Graz, Austria
**andreas.truegler@uni-graz.at*

F. Javier García de Abajo

ICFO — Institut de Ciencies Fotoniques,
The Barcelona Institute of Science and Technology,
08860 Castelldefels, Barcelona, Spain

ICREA — Institució Catalana de Recerca i Estudis Avançats,
Passeig Lluís Companys 23, 08010 Barcelona, Spain

Received 5 July 2017
Accepted 14 August 2017
Published 15 September 2017

Spatial nonlocality in the photonic response of metallic nanoparticles is actually known to produce near-field quenching and significant plasmon frequency shifts relative to local descriptions. As the control over size and morphology of fabricated nanostructures is truly reaching the nanometer scale, understanding and accounting for nonlocal phenomena is becoming increasingly important. Recent advances clearly point out the need to go beyond the local theory. We here present a general formalism for incorporating spatial dispersion effects through the hydrodynamic model and generalizations for arbitrary surface morphologies. Our method relies on the boundary element method, which we supplement with a nonlocal interaction potential. We provide numerical examples in excellent agreement with the literature for individual and paired gold nanospheres, and critically examine the accuracy of our approach. The present method involves marginal extra computational cost relative to local descriptions and facilitates the simulation of spatial dispersion effects in the photonic response of complex nanoplasmonic structures.

Keywords: Plasmonics; nonlocal effects; nanophotonics; nanoparticles; spatial dispersion; hydrodynamic model.

PACS numbers: 42.25.Gy, 42.50.Ct, 52.25.Os, 71.10.-w, 78.67.Bf

*Corresponding author.

1. Introduction

Plasmons sustained by sharp metal tips and narrow gaps between metallic nanostructures produce high levels of light intensity enhancement, as well as strong concentration of the optical electromagnetic field. This is the basis of applications such as optical detection with sensitivity down to single molecules.[1,2] Equally interesting is the nonlinear response associated with plasmons,[3] which opens new perspectives for nanoscale optical computation devices. Within a local description of the optical response based upon the use of frequency-dependent dielectric functions, the levels of field enhancement and confinement are found to indefinitely increase with decreasing gap distance or when the radius of curvature becomes increasingly small in sharp tips and corners. However, the assumption of local response breaks down at small distances due to Landau damping, a phenomenon associated with the excitation of electron–hole pairs and involving the exchange of wave vectors $> \omega/v_F$, where ω is the light frequency and v_F is the Fermi velocity (e.g., $v_F = 1.39\times10^6$ m/s in gold). The critical distance $\sim v_F/\omega$ is then of the order of the nanometer for visible and near-infrared light. As gap separations in the sub-nanometer regime are already being experimentally explored,[4–7] nonlocal effects cannot be ignored. The spill out of the valence electron density outside the metal is also taking place over sub-nanometer distances and produces further nonlocal effects. In general, nonlocality leads to plasmon blueshifts relative to a local description in these materials,[7–11] as well as plasmon broadening and significant reduction in the local field enhancement.[12] These phenomena are thus detrimental for plasmonic applications in which confinement and field enhancement are critical, particularly in sensing, and thus they become important at small distances of the order of the targeted molecules.[13]

A rigorous theoretical approach should involve the use of linear response theory combined with the electron wave functions of the metal structures under consideration. While this procedure gives analytical results in homogeneous bulk metals,[14,15] it becomes computationally involved even for the simple case of a planar interface.[8] Nevertheless, the nonlocal optical response of metal clusters has been investigated from first principles for small structures,[16] and strong emphasis has been recently placed on narrow gaps[17–20] and two-dimensional (2D) plasmonic materials such as graphene.[21,22] However, these methods are not computationally affordable for complex morphologies, which demand the development of alternative, simpler approaches to describe nonlocal effects.

A popular scheme for incorporating nonlocal effects is the hydrodynamic description,[23] which introduces a pressure term that inhibits squashing electrons into too small volumes at sharp features or hot-spots of plasmonic nanoparticles. This approach dates back to pioneering studies of surface plasmons[24,25] and has been recently used to study plasmons in metal nanoparticles by the Mortensen group,[26] including recent developments to include quantum corrections obtained from first-principles calculations[27] that capitalize on the Feibelman d-function formalism,[28] and has been applied to simple geometries such as spheres or nanorods. However,

implementations of nonlocal effects in generic Maxwell solvers, such as the finite difference time domain (FDTD),[29] finite element method (FEM),[30] or boundary element method (BEM)[31,32] are needed for the simulation of complex nanoparticle geometries.

In this paper, we present a first step towards the implementation of nonlocal effects in a generic Maxwell solver based on BEM, and introduce two different approaches. First, we follow Dasgupta and Fuchs,[33] who developed a solution scheme for nanospheres within the quasistatic approximation, and extend their method to generic nanoparticle geometries. Second, we adopt the approach of the Pendry group[34] to account for nonlocal effects within the hydrodynamic model by replacing the nonlocal metal by a local metal coated by a thin artificial layer, which both possess local permittivities chosen in order to give the same optical response as the nonlocal metal. We critically examine the advantages and disadvantages of these schemes for a metallic nanosphere, where analytic solutions are available, and then continue to prove the applicability of our implementation for the more complicated example of coupled nanoparticles.

2. Theory

2.1. *Specular-reflection model*

In this paper, we consider metallic nanoparticles embedded in a dielectric background with permittivity ε_b. As for the metal, we assume a linear but nonlocal response, where the dielectric displacement $\mathbf{D}(\mathbf{r},\omega)$ at point $\mathbf{r}$ is related to the electric field $\mathbf{E}(\mathbf{r}',\omega)$ at position $\mathbf{r}'$ via

$$\mathbf{D}(\mathbf{r},\omega) = \int \varepsilon(\mathbf{r}-\mathbf{r}',\omega)\mathbf{E}(\mathbf{r}',\omega)\, d^3r'. \tag{1}$$

Throughout this work, we consider Maxwell's equations in the frequency domain, with ω being the angular frequency. We use Gaussian units in what follows, and assume a homogeneous and isotropic dielectric function that only depends on the distance $|\mathbf{r}-\mathbf{r}'|$, rather than a general function $\varepsilon(\mathbf{r},\mathbf{r}',\omega)$ that could additionally account for modifications of the dielectric screening at the particle boundary.

We closely follow the approach of Dasgupta and Fuchs[33] using, however, a notation that is suited for generic nanoparticle shapes rather than only spherical ones. For sufficiently small nanoparticles, one can employ the quasistatic approximation[35] and neglect retardation effects in the optical response, while retaining the full frequency dependence in the permittivities $\varepsilon(\omega)$. The electric field can then be expressed in terms of a scalar potential $V(\mathbf{r},\omega)$ via $\mathbf{E}(\mathbf{r},\omega) = -\nabla V(\mathbf{r},\omega)$, and Gauss' law becomes

$$\nabla\cdot\mathbf{D}(\mathbf{r},\omega) = -\nabla\cdot\int \varepsilon(\mathbf{r}-\mathbf{r}',\omega)\nabla V(\mathbf{r}',\omega)\, d^3r' = 4\pi\rho(\mathbf{r},\omega), \tag{2}$$

with $\rho(\mathbf{r},\omega)$ being the free charge distribution.[36] To solve Eq. (2), we introduce the Green function $G_{\mathrm{nl}}(\mathbf{r}-\mathbf{r}',\omega)$ of the unbounded nonlocal metal, which is defined

through

$$\nabla \cdot \int \varepsilon(\mathbf{r}-\mathbf{r}_1,\omega)\nabla G_{\rm nl}(\mathbf{r}_1-\mathbf{r}',\omega)\, d^3r_1 = -4\pi\delta(\mathbf{r}-\mathbf{r}'). \tag{3}$$

As discussed in Appendix A, the Green function can be evaluated as

$$G_{\rm nl}(\mathbf{r},\omega) = \frac{2}{\pi}\int_0^\infty \frac{1}{\varepsilon(q,\omega)}\frac{\sin qr}{qr}\, dq\,, \tag{4}$$

with $\varepsilon(q,\omega)$ being the Fourier transform of the real space permittivity $\varepsilon(\mathbf{r},\omega)$ and q being a wave number. Equation (4) allows us to compute the Green function for any kind of dielectric model, including the hydrodynamic one, which we use exclusively below, but also for the Lindhard or Mermin ones,[37,38] which have a longstanding tradition in solid-state physics.

In a boundary integral method approach, we consider a metallic particle with volume Ω and relate the scalar potential V_1 inside the particle to the surface charge distribution $\sigma_1(\mathbf{s},\omega)$ through[31]

$$V_1(\mathbf{r},\omega) = \int_{\partial\Omega} G_{\rm nl}(\mathbf{r}-\mathbf{s}',\omega)\sigma_1(\mathbf{s}',\omega)\, d^2s', \tag{5}$$

where the integral extends over the particle boundary $\partial\Omega$. Correspondingly, the potential outside the particle can be expressed as

$$\varepsilon_b V_2(\mathbf{r},\omega) = \int_{\partial\Omega} G_0(\mathbf{r}-\mathbf{s}',\omega)\sigma_2(\mathbf{s}',\omega)\, d^2s' + V_{\rm ext}(\mathbf{r},\omega), \tag{6}$$

with $V_{\rm ext}(\mathbf{r},\omega)$ being the electrostatic potential created by an external excitation, such as a plane wave or a swift electron, and the free-space Green function $G_0(r) = \frac{1}{r}$ defined in such a way that it satisfies $\nabla^2 G_0(\mathbf{r}-\mathbf{r}') = -4\pi\delta(\mathbf{r}-\mathbf{r}')$. Note that the above definitions somewhat differ from previous work[31,32] and are needed because the definition of the nonlocal Green function in Eq. (3) explicitly incorporates the dielectric function.

To compute the unknown surface charge distributions $\sigma_{1,2}$ at the particle boundary, we have to invoke the customary electric boundary conditions. The continuity of the tangential electric field can be achieved with $V_1 = V_2$ at the particle boundary. For the continuity of the normal component of the dielectric displacement, we use $\mathbf{D}_2(\mathbf{r},\omega) = -\varepsilon_b\nabla V_2(\mathbf{r},\omega)$ together with

$$\mathbf{D}_1(\mathbf{r},\omega) = -\nabla\int_{\partial\Omega} G_0(\mathbf{r}-\mathbf{s}')\sigma_1(\mathbf{s}',\omega)\, d^2s'. \tag{7}$$

The latter equality can be proven by taking the divergence on both sides of Eq. (7) as well as Eq. (1), and using the defining equations for the Green functions $G_{\rm nl}$ and G_0. When approaching $\mathbf{r}\to\mathbf{s}$ in Eq. (7) towards the boundary, we obtain for the normal component of the dielectric displacement[31]

$$\hat{\mathbf{n}}\cdot\mathbf{D}(\mathbf{s},\omega) = \pm 2\pi\sigma(\mathbf{s},\omega) - \int_{\partial\Omega} F_0(\mathbf{s}-\mathbf{s}')\sigma_1(\mathbf{s}',\omega)\, d^2s', \tag{8}$$

where $\hat{\mathbf{n}}$ is a unit vector pointing along the direction of the outer surface normal of the boundary $\partial\Omega$, the sign depends on whether we approach the boundary from the outside (+) or inside (−), and $F_0 = (\hat{\mathbf{n}} \cdot \nabla) G_0$.

2.1.1. *BEM approach*

In the BEM approach,[31,32] one approximates the particle boundary by boundary elements of finite size, such as triangles or quadrilaterals, and uses for the surface charge distributions within each element a constant value (collocation method, used in this work) or some interpolation scheme (Galerkin method). In the collocation BEM approach, the surface charge distributions σ become vectors with the same dimension n as the number of boundary elements, and the Green functions G become matrices of dimension $n \times n$.

Within such an approach, the continuity of the potential and the normal displacement at the boundary can be expressed as

$$\varepsilon_b G_{\mathrm{nl}} \sigma_1 = G_0 \sigma_2 + V_{\mathrm{ext}}, \tag{9a}$$

$$(F_0 + 2\pi \mathbb{1}) \sigma_1 = (F_0 - 2\pi \mathbb{1}) \sigma_2 + V'_{\mathrm{ext}}\,, \tag{9b}$$

where V'_{ext} denotes the derivative $(\hat{\mathbf{n}} \cdot \nabla) V_{\mathrm{ext}}$ of the external potential in the direction of the surface normal, and $\mathbb{1}$ is the unit matrix. Equations (9) provide two coupled equations for the unknowns σ_1 and σ_2, which can be solved as follows:

$$\sigma_2 = \left[(F_0 + 2\pi \mathbb{1}) \frac{G_{\mathrm{nl}}^{-1}}{\varepsilon_b} - (F_0 - 2\pi \mathbb{1}) \right]^{-1} \left[V'_{\mathrm{ext}} - (F_0 + 2\pi \mathbb{1}) \frac{G_{\mathrm{nl}}^{-1}}{\varepsilon_b} V_{\mathrm{ext}} \right]. \tag{10}$$

Once σ_2 is known, we can compute through Eq. (6) the potential as well as the electric field outside the particle, and we can in turn evaluate optical cross-sections for plane wave excitation or electron energy-loss probabilities for swift-electron excitation using well-known expressions.[31,32] An approach similar to ours has been also presented elsewhere.[39]

2.1.2. *Spherical nanoparticle*

For plane wave excitation, Dasgupta and Fuchs[33] explicitly evaluated the plasmonic response for a metallic nanosphere. We here briefly summarize the pertinent equations which will be used below to evaluate the accuracy of our BEM approach. For details, the interested reader is referred to Ref. 33. Within the approach discussed above, the authors derived the following expression for the polarizability of a metallic nanosphere:

$$\alpha(\omega) = a^3 \left[\frac{1 - F(a)}{1 + 2F(a)} \right], \quad F(r) = \frac{6a}{\pi} \int_0^\infty \frac{j_1(qr) j_1(qa)}{\varepsilon(q, \omega)}\, dq. \tag{11}$$

Here, a and j_1 are the radius of the sphere and the spherical Bessel function of first-order, respectively, and we have set $\varepsilon_b = 1$. Dasgupta and Fuchs continue to

analyze the "additional boundary conditions" (ABCs) underlying Eq. (11), which are found to be similar to the conditions of Fuchs and Kliewer[40] in the sense that the effect of the boundary is assumed to be the same as that of a fictitious medium which is an "image" of the real system.

An equivalent approach was pioneered by Ritchie and Marusak[50] to study nonlocal effects on the dispersion relation of surface plasmons in a flat metal surface, invoking a microscopic model in which conduction electrons were specularly reflected at the surface, thus giving rise to the term *it specular-reflection model*.

However, the ABCs do not satisfy the condition that the normal component of the polarization vector vanishes at the boundary. For the special geometry of a sphere, this difficulty can be overcome by replacing Eq. (11) with a corrected version

$$\alpha(\omega) = a^3 \left[\frac{1 - \ F(a) + K(\varepsilon_L - 1)}{1 + 2F(a) + K(\varepsilon_L + 2)} \right], \quad K = \frac{\varepsilon_0 a \left[\frac{dF(r)}{dr} \right]_{r=a} - 1}{\varepsilon_L - \varepsilon_0}, \tag{12}$$

where $\varepsilon_L = \varepsilon(0, \omega)$ and ε_0 is the background dielectric constant of the sphere (see discussion below). With this correction, the component of the polarization vector vanishes at the boundary, but not its derivative. We return to this point in Sec. 3.

2.2. *Hydrodynamic model*

The hydrodynamic model provides a practical scheme for incorporating spatial dispersion in a metal. Within linear response theory, it describes the valence electron gas as a classical plasma which is modeled through the hydrodynamic equation[41]

$$i(\omega + i\gamma)\mathbf{J}_{\rm ind}(\mathbf{r}, \omega) = \nabla[\beta^2 \rho_{\rm ind}(\mathbf{r}, \omega)] - \frac{\omega_p^2}{4\pi}\mathbf{E}(\mathbf{r}, \omega), \tag{13}$$

where $\mathbf{J}_{\rm ind}$ and $\rho_{\rm ind}$ are the induced current and charge densities, ω_p is the classical plasma frequency, $\mathbf{E}$ is the local electric field, and γ is a phenomenological damping rate. The β^2 term describes the hydrodynamic pressure, which introduces nonlocality in our model. Equation (13) has to be combined with the continuity equation $\nabla \cdot \mathbf{J}_{\rm ind} = i\omega\rho_{\rm ind}$ and Poisson's equation $\nabla \cdot \varepsilon_0 \mathbf{E} = 4\pi(\rho_{\rm ext} + \rho_{\rm ind})$ to yield a nonlocal momentum- and frequency-dependent dielectric function for the bulk metal,

$$\varepsilon(q, \omega) = \varepsilon_0 - \frac{\omega_p^2}{\omega(\omega + i\gamma) - \beta^2 q^2}\,. \tag{14}$$

Here, ε_0 is a background dielectric constant, associated with bound electrons in the metal (such as *d*-band electrons in the transition metals Au or Ag), which in principle can also depend on frequency.

An advantage of the hydrodynamic model is that it is relatively simple and allows us to derive analytic expressions in many cases of interest. For instance, one can work out the Green function of Eq. (4) to get

$$G_{\rm nl}(\mathbf{r}) = \frac{1}{\varepsilon_L r} + \left(\frac{1}{\varepsilon_0} - \frac{1}{\varepsilon_L} \right) \frac{e^{-\lambda r}}{r}, \quad \lambda = \frac{\omega_p}{\beta} \sqrt{\frac{1}{\varepsilon_0} - \frac{1}{\varepsilon_0 - \varepsilon_L}}\,, \tag{15}$$

where for simplicity, we have not indicated the frequency dependence of the various quantities.

2.2.1. *Spherical nanoparticle*

For a spherical particle and the dielectric model of Eq. (13), one can also solve Maxwell's equations within the quasistatic approximation, and one obtains for the polarizability[10,34]

$$\alpha(\omega) = a^3 \left[\frac{\varepsilon_L - \varepsilon_B(1+\delta)}{\varepsilon_L + 2\varepsilon_B(1+\delta)} \right] \tag{16}$$

with

$$\delta = \left(\frac{\varepsilon_L}{\varepsilon_0} - 1 \right) \frac{j_1(x)}{x j_1'(x)}, \quad Q = \sqrt{\omega_p^2/\varepsilon_0 - \omega(\omega + i\gamma)}/\beta,$$

where $x = -i\,Qa$. Also, the $F(r)$ term of the Dasgupta and Fuchs model can be evaluated analytically and one arrives at Eq. (42) of Ref. 33. We come back to these expressions in Sec. 3.

2.2.2. *Artificial coating layer*

In Luo *et al.*,[34] the authors analyze the response function of metallic slabs, infinite cylinders, and spheres described by the hydrodynamic model of Eq. (13), and proposed a simplified description scheme consisting of (i) a metallic nanoparticle described by a local permittivity $\varepsilon_L(\omega) = \varepsilon(0, \omega)$, but (ii) covered by a thin artificial coating layer of thickness d with (local) permittivity

$$\varepsilon_t = \frac{\varepsilon_L \varepsilon_b}{\varepsilon_L - \varepsilon_b}\, Qd\,, \tag{17}$$

where Q is an effective wave number is related to the hydrodynamic β parameter. For sufficiently small d values, the optical response of the hydrodynamic model and the simplified local description scheme with an artificial coating layer can be shown to give almost indistinguishable results. Note that for a sphere, ε_t contain an additional radius-dependent scaling factor [see Eq. (2) of Ref. 34], which we neglect here for simplicity.

The above scheme is also expected to work for more complicated nanoparticle geometries, thus making the approach attractive for Maxwell solvers using only local dielectric permittivities, such as FDTD, FEM or BEM solvers. In addition, this approach works not only in the quasistatic regime, but it can also be directly incorporated in the full solution of Maxwell's equations including retardation. We return to this point in more detail below.

3. Results

3.1. *BEM implementation*

We have implemented the specular-reflection model[33] and the artificial coating layer model[34] in the Matlab toolbox MNPBEM,[32,42,43] which is a generic Maxwell solver using the methodology of Ref. 31. In the following, we only comment on the modifications with respect to the existing software.

In a first step, we have to compute the nonlocal Green function of Eq. (4). In particular, the term $\sin(qr)$ with its strong oscillations for large r values has to be treated with care. Our implementation relies on a spline interpolation[44] of $\varepsilon^{-1}(q,\omega)$ on a sufficiently dense q grid, which in each interval $[q_\mu, q_{\mu+1}]$ of the grid is expanded in a power series, and the resulting expressions

$$I_\mu^n(r) = \int_{q_\mu}^{q_{\mu+1}} \frac{\sin qr}{q} q^n \, dq$$

are then evaluated analytically. We find it convenient to store I_μ^n for selected distances on an equidistant r grid, without the additional r^{-1} factor showing up in Eq. (4), and to interpolate between the tabulated values when computing $G_{\rm nl}$. For the situations investigated in this paper, the computation of $G_{\rm nl}$ is very fast and accurate, as verified by comparing the results for the hydrodynamic model with those of Eq. (15).

Another critical point is the evaluation of the Green function matrix $G_{{\rm nl},ii}$ for diagonal boundary elements and elements that are sufficiently close to each other. Because of the short-range $e^{-\lambda r}/r$ term in Eq. (15), or similar short-range contributions for different dielectric screening models, the integration within a given boundary element $\partial\Omega_i$

$$G_{{\rm nl},ii} = \int_{\partial\Omega_i} \frac{g(|\mathbf{s}_i - \mathbf{s}'|)}{|\mathbf{s}_i - \mathbf{s}'|} d^2 s' = \int_0^{2\pi} d\phi' \int_0^{R_i(\phi')} d\rho' g(\rho')$$

has to be performed in polar coordinates with sufficiently high accuracy. In the above expression, we have assumed a nonlocal Green function of the form $g(\rho)/\rho$, $\mathbf{s}_i$ denotes the centroid of the boundary element, and $R_i(\phi)$ is the radius measured with respect to $\mathbf{s}_i$. Additionally, integration between neighbor elements has to be performed with a sufficiently high number of integration points, which have to be selected on the basis of convergence tests. We find fast convergence once the number of integration points exceeds some threshold values, with typically 50 integration points in the radial direction and 10 in the azimuthal one.

Similarly, for the artificial coating layer simulations, we produce the layer by shifting the particle boundary by a small amount, typically in the range between 0.05 nm and 0.5 nm, in the direction of the outer surface normals. The Green function element between a boundary element i and its "twin" element i' is then

evaluated again in polar coordinates as

$$G_{0,ii'} = \int_{\partial\Omega_{i'}} \frac{1}{|\mathbf{s}_i - \mathbf{s}'|}\, d^2 s' = \int_0^{2\pi} d\phi' \int_0^{R_{i'}(\phi')} d\rho' \, \frac{\rho'}{|\mathbf{s}_i - \mathbf{s}'|},$$

which converges rapidly for an even smaller number of integration points. In our simulations, we always consider curved particle boundaries[43] for this kind of integration. Note that for the artificial coating layer simulations, we only have to consider G_0 because of the use of local dielectric functions. The computation of F_0 can be performed in a similar fashion.

3.2. *Single sphere*

We start by considering a single sphere with the nonlocal dielectric permittivity of Eq. (14). We use the same material parameters as in Ref. 34, namely $\varepsilon_0 = 1$, $\omega_p = 3.3$ eV, $\gamma = 0.165$ eV, and $\beta = 0.0036c$, where c is the speed of light. These parameters mimic the dielectric response of gold. Note that in Refs. 12 and 45, a more general approach is introduced which also allows us to incorporate d band effects.

Figure 1 shows the results for metallic nanospheres with diameters of (a) 2.9 nm and (b) 5.4 nm. The dashed line presents results for a local dielectric function $\varepsilon_L(\omega) = \varepsilon(0, \omega)$ and the dashed-dotted line corresponds to results for the nonlocal BEM simulation based on Eq. (10). It is clear that nonlocailty leads to a significant blueshift of the plasmon resonance, particularly for the smaller sphere, in agreement with previous work.[12,26,33,34] The + symbols report results of the analytic model of Dasgupta and Fuchs,[33] which is in perfect agreement with our BEM simulations.

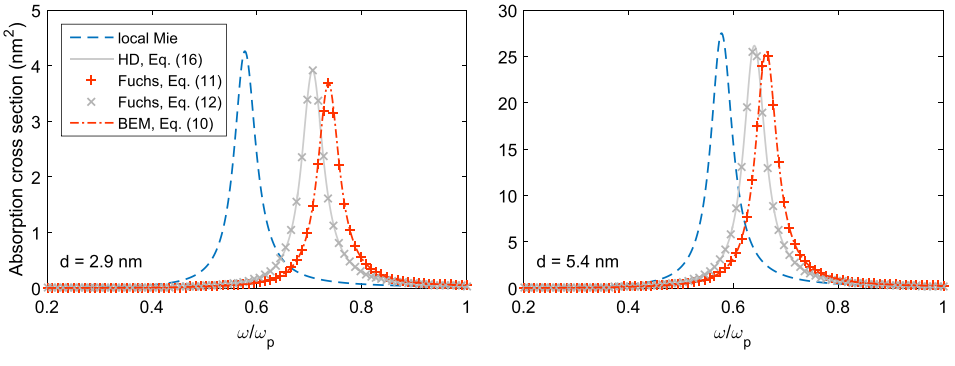

(a) (b)

Fig. 1. (Color online) Absorption cross-section of a nanosphere using the hydrodynamic model, for parameters given in text. The dashed line shows results for a local dielectric function $\varepsilon_L(\omega) = \varepsilon(0, \omega)$, the gray solid line is the exact solution for the hydrodynamic model of Eq. (16) in the quasistatic limit, and the dashed-dotted line is the result of a nonlocal BEM simulation using Eq. (10). The symbols show results of the model of Dasgupta and Fuchs without (+) and with (×) polarization corrections. We set $\varepsilon_b = 1$ and use sphere diameters of (a) 2.9 nm and (b) 5.4 nm.

When comparing the results to the exact nonlocal Mie solution of Eq. (16), solid line, we observe a slight discrepancy which can be traced back to the polarization vector $\mathbf{P}$ at the particle boundary. Within the description scheme of Eq. (10), which is based on the specular-reflection model of Ref. 33 without corrections, Eq. (11), $\hat{\mathbf{n}} \cdot \mathbf{P}$ does not vanish at the boundary. In contrast, the corrected version of Eq. (12) gives results (see symbols $\times$) in perfect agreement with the exact hydrodynamic result, demonstrating the importance of the condition $\hat{\mathbf{n}} \cdot \mathbf{P} = 0$ at the boundary. Quite generally, the deviations of the specular-reflection model from the exact result are rather small and the model has been used extensively in the literature.[12,45,46] Nevertheless, for an accurate modeling, the condition $\hat{\mathbf{n}} \cdot \mathbf{P} = 0$ has to be properly fulfilled, using for instance the methodology of Ref. 47. Such an approach is the subject of ongoing research and will be presented elsewhere.

Figure 2 shows the simulation results for the artificial coating layer model described in Sec. 2.2.2 using local permittivities for both metal and coating layers. Here, the absorption cross-section of the BEM approach (see + symbols), agrees perfectly with the exact hydrodynamic solution of Eq. (16). In a sense, this is not surprising because the artificial coating layer model is constructed in such a way that it gives the same results as the hydrodynamic model. Nevertheless, as already briefly discussed above, things are slightly more complicated because of our neglect of the radius-dependent factors in the permittivity, see also Eq. (2) of Ref. 34. The small influence of curvature on the permittivity of the artificial coating layer is in agreement with Luo *et al.*[34] Thus, we conclude that for nonlocal hydrodynamic simulations, the artificial coating layer model provides an excellent approach that can be easily implemented in Maxwell BEM solvers. In the following, we show the artificial coating layer simulations, but we remark that simulations using the specular-reflection model do not lead to significantly different results.

3.3. *Coupled spheres*

Figure 3 shows simulations for coupled nanospheres with a diameter of 8 nm and different gap distances. We use the same local and nonlocal dielectric models as in Figs. 1 and 2, but consider electron energy loss spectroscopy (EELS) simulations,[31,38,42] in which the plasmonic modes are probed by the energy losses experienced by an electron beam. The impact parameters of the electrons are indicated in the inset. In contrast to optical excitation, EELS spectra are usually less affected by specific selection rules and one can thus observe more modes.

In the local spectra, Fig. 3(a), we observe for decreasing gap distance a redshift of the dipolar bonding mode (see dashed line) and a splitting of the multipolar modes into a broad distribution (blue spectra). Note that for the smallest gap distances under consideration, electron tunneling might play some role,[19,48,49] which is here neglected for simplicity. In comparison, the nonlocal model predicts a less pronounced redshift of the dipole mode and a strong modification of the broad

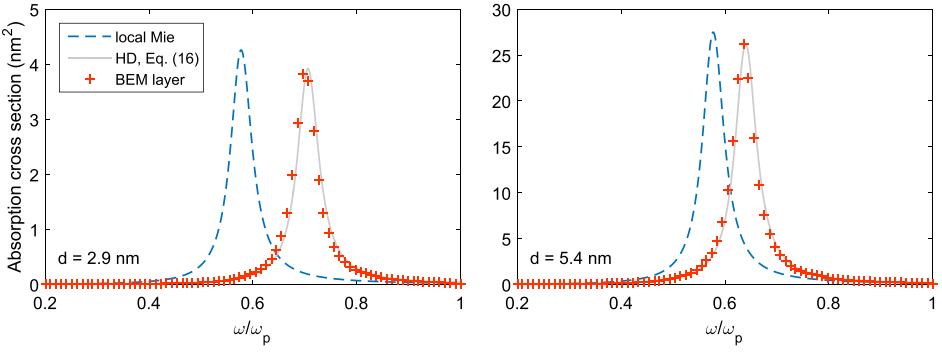

Fig. 2. (Color online) Same as Fig. 1 but showing results of BEM simulations for an artificial coating layer with a thickness 0.05 nm and the permittivity of Eq. (17).

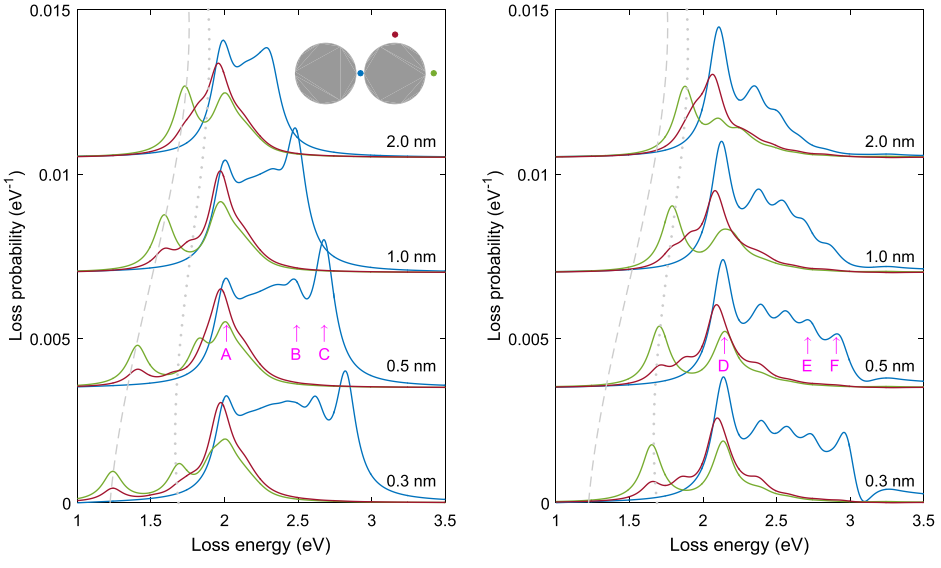

Fig. 3. (Color online) EELS spectra for coupled nanospheres with 8 nm diameter and varying gap distances (see annotation in figure); for (a) local and (b) nonlocal dieletric models. We use the same permittivities as in Figs. 1 and 2. The impact parameters of the electron beam are indicated in the inset. Spectra for different gap distances are offset for clarity. Dashed and dotted lines are guides to the eye for the energy position of the bonding dipole mode in the local and nonlocal models, respectively, and the arrows indicate the energy positions for the EELS maps of Fig. 4.

distribution associated with the multipolar modes. Both of these findings are in agreement with previous related studies..[12,26,34,45]

Figure 4 shows the EELS maps for the loss energies indicated in Fig. 3. One observes that for the largest loss energies, panels (C, F), the loss probability is

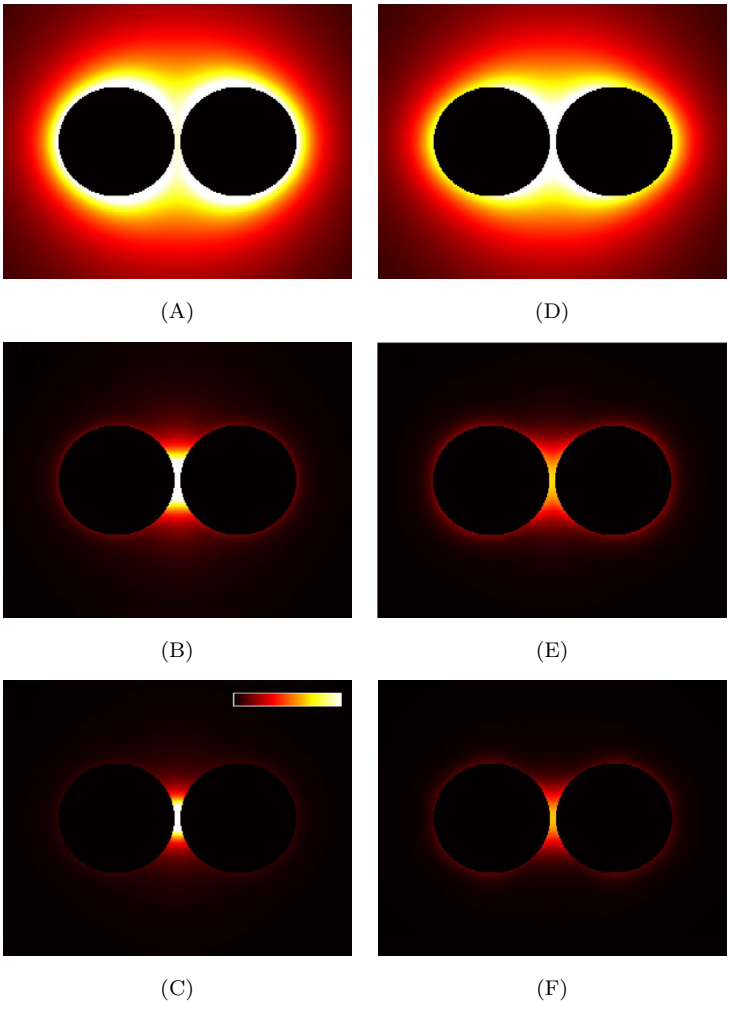

Fig. 4. (Color online) EELS maps for (A–C) local and (D–F) nonlocal simulations, at the loss energies indicated with arrows in Fig. 3 (in order of increasing energy). In the inset of panel (C), we show the color bar. Each of the maps (A–C) is scaled to its respective maximum, with identical color ranges for panels (A, D), (B, E), and (C, F).

strongly peaked in the gap region. However, the loss in that region has a much larger probability in the local simulation than in the nonlocal one. We attribute this to the pressure term proportional to β^2 in Eq. (13), which inhibits squashing electrons into too small volumes in the hot spot between the two spheres. A similar behavior is observed in panels (B, E).

4. Summary

In brief, we have presented two models for simulating nonlocal screening effects within the BEM approach: the specular-reflection model developed by Dasgupta

and Fuchs,[33] which builds on the nonlocal Green function for a generic nonlocal dielectric function, and the artificial coating layer model of Luo and coworkers[34] that mimics the effects of the hydrodynamic model by simulating metallic nanoparticles with local permittivities, but covered by a thin artificial coating layer that generates the correct reflection and transmission coefficients of the fields. We have shown that both models can be easily implemented, with a few modifications for more refined boundary integrations.

As for the specular-reflection model, we have discussed that further improvements are needed to provide full agreement with the exact Mie results of the hydrodynamic model. We find small deviations between the two approaches that have been traced back to the normal component of the polarization vector, which does not necessarily vanish at the particle boundary. As for the artificial coating layer model, we have found excellent agreement with the hydrodynamic Mie results. Quite generally, both approaches can be easily extended to the solution of the full Maxwell equations and to simulations of more complex nanostructures. Future work will additionally address the question of how to combine electrodynamic simulations with *ab initio* simulations for the pertinent nonlocality parameters, thus extending the applicability of Maxwell solvers to sharp features and narrow gap regions where quantum corrections are expected to be of crucial importance.

Acknowledgments

We are grateful to Christin David for most helpful discussions. This work has been supported in part by the Austrian Science Fund FWF under project P27299-N27 and the SFB F49 NextLite (F4906-N23), and by NAWI Graz. FJGA acknowledges support from the Spanish MINECO (MAT2014-59096-P and SEV2015-0522), and AGAUR (2014 SGR 1400).

Appendix A

In this appendix, we show how to derive Eq. (4) for the Green function of the nonlocal medium. We first introduce the spatial Fourier transform and its inverse,

$$\tilde{G}_{\mathrm{nl}}(\mathbf{q},\omega) = \int e^{-i\mathbf{q}\cdot\mathbf{r}} G_{\mathrm{nl}}(\mathbf{r},\omega)\, d^3r, \tag{A.1}$$

$$G_{\mathrm{nl}}(\mathbf{r},\omega) = (2\pi)^{-3} \int e^{i\mathbf{q}\cdot\mathbf{r}} \tilde{G}_{\mathrm{nl}}(\mathbf{q},\omega)\, d^3q. \tag{A.2}$$

The convolution of the dielectric and Green functions appearing in Eq. (3) can then be brought to the form

$$\int \varepsilon(\mathbf{r}-\mathbf{r}_1,\omega)\nabla G_{\mathrm{nl}}(\mathbf{r}_1-\mathbf{r}',\omega)\, d^3r_1 = (2\pi)^{-3} \int e^{i\mathbf{q}\cdot(\mathbf{r}-\mathbf{r}')} i\mathbf{q}\, \varepsilon(\mathbf{q},\omega)\, \tilde{G}_{\mathrm{nl}}(\mathbf{q},\omega)\, d^3q.$$

The term $i\mathbf{q}$ stems from the derivative ∇ of the Green function. Inserting this expression into Eq. (3) and using the wave vector decomposition $\delta(\mathbf{r}) = (2\pi)^{-3}$

$\int e^{i\mathbf{q}\cdot\mathbf{r}}\, d^3q$, we find

$$\tilde{G}_{\rm nl}(\mathbf{q},\omega) = \frac{4\pi}{q^2}\frac{1}{\varepsilon(q,\omega)}.$$

Thus, we get in spherical coordinates

$$G_{\rm nl}(\mathbf{r},\omega) = \frac{1}{4\pi^2}\int_0^\infty \left(\int_0^\pi e^{iqr\cos\theta}\,\sin\theta d\theta\right)\left(\frac{4\pi}{q^2}\frac{1}{\varepsilon(q,\omega)}\right) q^2 dq,$$

which finally leads to Eq. (4) of the main text.

References

1. H. Xu *et al.*, *Phys. Rev. Lett.* **83**, 4357 (1999).
2. L. Rodriguez-Lorenzo *et al.*, *J. Am. Chem. Soc.* **131**, 4616 (2009).
3. M. Danckwerts and L. Novotny, *Phys. Rev. Lett.* **98**, 026104 (2007).
4. S. Bidault, F. J. García de Abajo and A. Polman, *J. Am. Chem. Soc.* **130**, 2750 (2009).
5. J. B. Lattiser *et al.*, *Nano Lett.* **8**, 1212 (2009).
6. K. J. Savage *et al.*, *Nature* **491**, 574 (2012).
7. C. Ciracì *et al.*, *Science* **337**, 1072 (2012).
8. A. Liebsch, *Phys. Rev. B* **48**, 11317 (1993).
9. J. A. Scholl, A. L. Koh and J. A. Dionne, *Nature* **483**, 421 (2012).
10. S. Raza *et al.*, *Opt. Express* **21**, 27344 (2013).
11. T. V. Teperik *et al.*, *Phys. Rev. Lett.* **110**, 263901 (2013).
12. F. J. García de Abajo, *J. Phys. Chem. C* **112**, 17983 (2008).
13. G. W. Ford and W. H. Weber, *Phys. Rep.* **113**, 195 (1984).
14. J. Lindhard, *K. Dan. Vidensk. Selsk. Mat.-Fys. Medd.* **28**, 1 (1954).
15. N. Mermin, *Phys. Rev. B* **1**, 2362 (1970).
16. G. Onida, L. Reining and A. Rubio, *Rev. Mod. Phys.* **74**, 601 (2002).
17. J. Zuloaga, E. Prodan and P. Nordlander, *Nano Lett.* **9**, 887 (2009).
18. J. Zuloaga, E. Prodan and P. Nordlander, *ACS Nano* **4**, 5269 (2010).
19. R. Esteban *et al.*, *Nat. Commun.* **3**, 825 (2012).
20. D. Marinica *et al.*, *Nano Lett.* **12**, 1333 (2012).
21. S. Thongrattanasiri, A. Manjavacas and F. J. García de Abajo, *ACS Nano* **6**, 1766 (2012).
22. S. Thongrattanasiri *et al.*, *Laser Photon. Rev.* **7**, 297 (2013).
23. K. S. Singwi and M. P. Tosi, *Solid State Phys.* **36**, 177 (1981).
24. R. H. Ritchie, *Phys. Rev.* **106**, 874 (1957).
25. F. Fujimoto and K. Komaki, *J. Phys. Soc. Jap.* **25**, 1679 (1968).
26. S. Raza *et al.*, *J. Phys., Condens. Matter* **27**, 183204 (2015).
27. T. Christensen *et al.*, *Phys. Rev. Lett.* **118**, 157402 (2017).
28. P. J. Feibelman, *Prog. Surf. Sci.* **12**, 287 (1982).
29. A. Taflove and S. C. Hagness, *Computational Electrodynamics* (Artech House, Boston, 2005).
30. J. S. Hesthaven, *Adv. Imaging Electron Phys.* **127**, 59 (2003).
31. F. J. García de Abajo and A. Howie, *Phys. Rev. B* **65**, 115418 (2002).
32. U. Hohenester and A. Trügler, *Comput. Phys. Commun.* **183**, 370 (2012).
33. B. B. Dasgupta and R. Fuchs, *Phys. Rev. B* **24**, 554 (1981).
34. Y. Luo *et al.*, *Phys. Rev. Lett.* **111**, 093901 (2013).
35. S. A. Maier, *Plasmonics: Fundamentals and Applications* (Springer, Berlin, 2007).

36. J. D. Jackson, *Classical Electrodynamics* (Wiley, New York, 1999).
37. G. D. Mahan, *Many-Particle Physics* (Plenum, New York, 1981).
38. F. J. García de Abajo, *Rev. Mod. Phys.* **82**, 209 (2010).
39. A. Hildebrandt *et al.*, *Phys. Rev. Lett.* **93**, 108104 (2004).
40. K. L. Kliewer and R. Fuchs, *Phys. Rev.* **172**, 607 (1968).
41. F. Bloch, *Z. Phys.* **81**, 363 (1933).
42. U. Hohenester, *Comput. Phys. Commun.* **185**, 1177 (2014).
43. J. Waxenegger, A. Trügler and U. Hohenester, *Comput. Phys. Commun.* **193**, 138 (2015).
44. W. H. Press *et al.*, *Numerical Recipes in C++: The Art of Scientific Computing*, 2nd edn. (Cambridge University Press, Cambridge, 2002).
45. C. David and F. J. García de Abajo, *J. Phys. Chem. C* **115**, 19470 (2011).
46. R. Ruppin, *Phys. Rev. B* **45**, 11209 (1992).
47. W. Yan, N. A. Mortensen and M. Wubs, *Phys. Rev. B* **88**, 155414 (2013).
48. U. Hohenester, *Phys. Rev. B* **91**, 205436 (2015).
49. W. Zhu *et al.*, *Nat. Commun.* **7**, 11495 (2016).
50. R. H. Ritchie and A. L. Marusak, *Surf. Sci.* **4**, 234 (1966).